Electronic Supplementary Information

A cubane-type manganese complex with H_2O oxidation capabilities

Swetanshu Tandon,[a,b] Joaquín Soriano-López,[a,b] Amal C. Kathalikkattil,[a,b] Guanghua Jin,[a,b] Paul Wix,[a,b] Munuswamy Venkatesan,[c] Ross Lundy,[a,b] Michael A. Morris,[a,b] Graeme W. Watson*[a] and Wolfgang Schmitt[a,b]*

[a] School of Chemistry & CRANN Institute, University of Dublin, Trinity College, Dublin 2, Ireland.

[b] AMBER Centre, University of Dublin, Trinity College, Dublin 2, Ireland.

[c] School of Physics & CRANN Institute, University of Dublin, Trinity College, Dublin 2, Ireland.

Correspondence to: watsong@tcd.ie, schmittw@tcd.ie.

Contents

Experimental Methods

General Considerations

All chemicals mentioned were used as obtained from standard commercial sources. All manipulations were performed under aerobic conditions.

Synthesis of $[K_2Mn_8(\mu_3\text{-}O)_4(\mu\text{-}OH)_2((CH_3)_3CCOO)_{16}(CH_3CN)_2]\cdot CHCl_3$ (**Mn_8K_2**)

$KMnO_4$ (0.079 g, 0.5 mmol) and pivalic acid (0.408 g, 4 mmol) were added to 20 mL of CH_3CN. The solution was refluxed for 2.5 hours. To the hot solution, 8 mL of $CHCl_3$ was added and the resultant was stirred for 5 minutes, filtered and left undisturbed for 1 day. Crystals were obtained within a day. The crystallisation was found to be dependent on the humidity and temperature and small variation in the $CH_3CN/CHCl_3$ ratio can lead to good quality crystals. The crystals were washed with $CH_3CN/CHCl_3$ (20/10 mL) mixture and dried. Yield: 32% (based on Mn).

Elemental Analysis

Elemental (C, H, N) analysis was performed using an Exeter Analytical CE 440 at the microanalytical laboratory at the School of Chemistry and Chemical Biology of University College Dublin, Belfield, Dublin, Ireland. Elemental analysis: $C_{85}H_{153}Cl_3K_2Mn_8N_2O_{38}$ – Calculated: C 41.92, H 6.33, N 1.15. Found: C 41.29, H 6.23, N 0.65.

Single-Crystal X-Ray Diffraction

A suitable crystal was selected and immersed in oil, mounted in a mitiGen loop on a Bruker APEX-II CCD diffractometer. The crystal was kept at 99.99 K during data collection using an Oxford Cryostream low- temperature device. The diffraction frames were integrated and processed using the Bruker SAINT software package. The data were corrected for absorption effects using the multi-scan method (SADABS).[1] Using Olex2,[2] the structure was solved with the XT[3] structure solution program using Intrinsic Phasing and refined with the XL[4] refinement package using Least Squares minimisation.

Powder X-Ray Diffraction (PXRD)

Powder XRD patterns for **Mn_8K_2** were measured using a glass capillary in Bruker APEX II diffractometer. The powdery crystalline sample was ground under $CH_3CN/CHCl_3$ mixture and was sealed inside a 0.5 mm diameter glass capillary with solvent to retain crystallinity and to avoid the loss of lattice solvent. The capillary was mounted on the holder using Blu Tack and centred on the goniometer head for data collection. The data was collected in Bruker APEX II diffractometer at 230 K using CuKα microfocus source (wavelength, 1.54184 Å) upon 360° ϕ rotational frames at 2θ values of 10° and 20°, with exposure times of 300 seconds per frame at a detector distance of 120 mm. Overlapping sections of the data were combined and the data were processed using the Bruker APEX II routine and the XRD2 -Eva subprogram. The experimental pattern does not account for sample-derived or instrumental broadening effects. To fit the data a Rietveld refinement comparing experimental powder and single-crystal X-ray diffraction data was conducted (see Fig. S1).

Thermogravimetric Analysis

Thermogravimetric analysis was performed using Perkin Elmer Pyris-1 Thermogravimetric analyser under a continuous flow of N_2. The measurement was carried out using freshly dried sample. The sample was held at 20 ˚C for 10 minutes. This was followed by heating up to 900 ˚C at 2 ˚C /minutes.

FTIR Analysis

Infrared spectroscopy measurements were performed on a PerkinElmer Spectrum one FT-IR spectrometer using a universal ATR sampling accessory. Data was collected and processed using Spectrum v5.0.1 (2002 PerkinElmer Instrument LLV) software. 8 scans were performed in the range of 4000 – 280 cm^{-1}.

Magnetic Measurements

Magnetic susceptibility measurement was carried out on a 5 T MPMS SQUID from Quantum Design using 17.6 mg of **Mn_8K_2**. Temperature dependence of magnetic susceptibility was measured in the temperature range of 2-300 K in an applied magnetic field of 0.1 T.

Scanning Electron Microscopy (SEM) and Energy Dispersive X-Ray (EDX) spectroscopy analysis

SEM was carried out on a Zeiss ULTRA plus scanning electron microscope using both InLens and SE2 detectors at a 5 kV acceleration voltage. EDX spectroscopy was carried out on samples within the microscope using a 20mm² Oxford Inca EDX detector and a 15 kV acceleration voltage.

For SEM and EDX spectroscopy analyses, crystals of **Mn_8K_2** and **Mn_8K_2*** were deposited on Si/SiO_2 wafers. Both samples were analysed using a Zeiss Ultra Plus scanning electron microscope.

Mass Spectrometry

Mass spectra were recorded using a Water Alliance Micromass LCT classic spectrometer.

XPS Analysis

X-ray photoelectron spectroscopy was performed under ultra-high vacuum condition ($<5 \times 10^{-10}$ mbar) using a VG Scientific ESCAlab Mk II system equipped with a hemispherical analyser using Al Kα X-rays (1486.6 eV). The emitted photoelectrons were collected at a take-off angle of 90 ° from the samples surface. The analyser pass energy was set to 100 eV for survey scans and 40 eV for high-resolution core scans, yielding an overall resolution of 1.5 eV. Photoemission peak positions were corrected to C 1s at a binding energy of 284.8 eV.

Electrochemistry

Electrochemical measurements were performed using a Biologic VSP potentiostat. The Ohmic drop was measured prior to each experiment and compensated using the positive feedback compensation as implemented in the instrument. The typical three-electrode set-up used for all the experiments was composed of Ag/AgCl (KCl 3M) reference electrode, modified carbon paste (**CP**) working electrodes (surface area = 0.07 cm^2), and a Pt mesh. All the measurements in aqueous media were carried out in a 50 mM potassium phosphate (KP$_i$) buffer solution with KNO_3 (1 M) as electrolyte at pH 7.2. The **CP** blends were prepared by mixing **CP** and the desired amount of catalyst in an agate mortar, then the mixtures were inserted inside the **CP** electrode pocket. The linear sweep voltammetry (LSV) measurements were conducted using an ALS RRDE-3A set-up with a **CP** rotating disc electrode (surface area = 0.07 cm^2) at 1,600 r.p.m., and at a scan rate of 1 mV s^{-1}. Tafel data were extracted from the LSV measurements. Bulk water electrolysis was performed using the same conditions as stated for the LSV measurements.

All the applied potentials (E_{app}) were converted to the normal hydrogen electrode (NHE) reference scale using $E_{NHE} = E_{Ag/AgCl} + 0.210(V)$. The overpotentials were calculated by subtracting the thermodynamic water oxidation potential ($E^0_{H_2O/O_2}$) to E_{app} as:

$$\eta = E_{app} - E^0_{H_2O/O_2}$$

Where $E^0_{H_2O/O_2}$ was corrected by the pH value employing the Nerst equation:

$$E^0_{H_2O/O_2} = 1.229 - (0.059 \times pH) \text{ (V) vs NHE at 25°C}$$

The geometrical area of the CP electrode was used to calculate all the current densities. The onset potentials were estimated from the intersection point between the tangent lines of the Faradaic current at 0.5 mA cm^{-2} and the non-Faradic current except in case of 10% **Mn_8K_2*** in which case the tangent lines of the Faradaic current at 0.35 mA cm^{-2} and the non-Faradic current was used.

For measurements in non-aqueous media, a saturated calomel electrode (SCE) was used as a reference electrode along with a Pt counter electrode. For the working electrode, a glassy carbon electrode was used and **Mn_8K_2** was mechanically deposited on the electrode surface. The measurements were conducted in an electrolyte solution of 0.1 M $Bu^n{}_4NPF_6$ in dry acetonitrile. Before the measurement, the solution was purged with N_2 to remove oxygen and during the measurements, the solution was kept under an atmosphere of N_2. The cyclic voltammograms were recorded at a scan rate of 100 mV/s. The reported potentials were converted to the normal hydrogen electrode (NHE) reference scale using $E_{NHE} = E_{SCE} + 0.244(V)$.

Table S1 Crystallographic information for $\mathbf{Mn_8K_2}$.

Empirical formula	$C_{85}H_{153}Cl_3K_2Mn_8N_2O_{38}$
Formula weight	2435.15
Temperature/K	99.99
Crystal system	monoclinic
Space group	$P2_1/n$
a/Å	19.040(2)
b/Å	15.7109(17)
c/Å	20.192(2)
α/°	90
β/°	100.691(2)
γ/°	90
Volume/Å^3	5935.3(11)
Z	1
ρ_{calc}g/cm^3	1.363
μ/mm^{-1}	1.033
F(000)	2540
Crystal size/mm^3	0.26 × 0.18 × 0.05
Radiation	MoKα (λ = 0.71073)
2Θ range for data collection/°	3.306 to 53.514
Index ranges	$-24 \le h \le 24$, $-19 \le k \le 19$, $-25 \le l \le 25$
Reflections collected	190941
Independent reflections	12589 [R_{int} = 0.0683, R_{sigma} = 0.0274]
Data/restraints/parameters	12589/103/749
Goodness-of-fit on F^2	1.063
Final R indexes [I>=2σ (I)]	R_1 = 0.0439, wR_2 = 0.1096
Final R indexes [all data]	R_1 = 0.0641, wR_2 = 0.1214
Largest diff. peak/hole / e Å^{-3}	1.02/-1.30

Table S2 Bond valance sum for **Mn_8K_2**.

Atom	*Bond Valance Sum*	*Assigned Oxidation State*
Mn1	3.217	+3
Mn2	3.171	+3
Mn3	3.190	+3
Mn4	3.147	+3

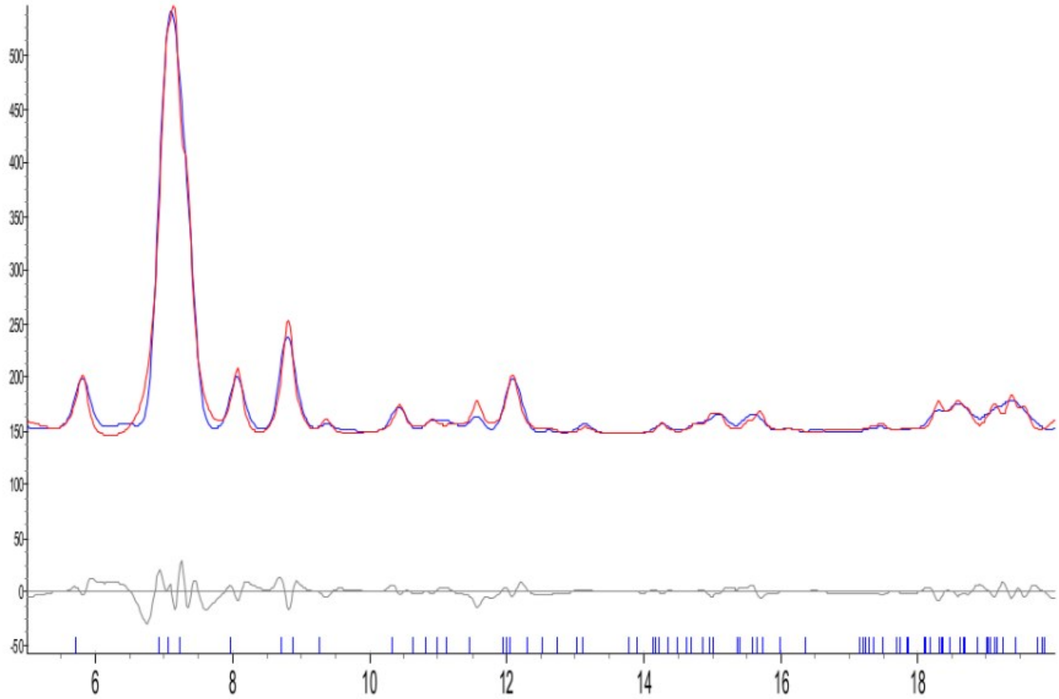

Fig. S1 Experimental PXRD pattern of a bulk sample of **Mn_8K_2** and a simulated pattern, based on the single-crystal X-ray diffraction data. Legend Information: experimental X-ray powder pattern (blue), fitted pattern (red), differential plot (grey), hkl lines (vertical blue lines). R_{wp} (weighted profile R factor) = 6.40 , validating the provided structural model and confirming the phase-purity of the sample.[5]

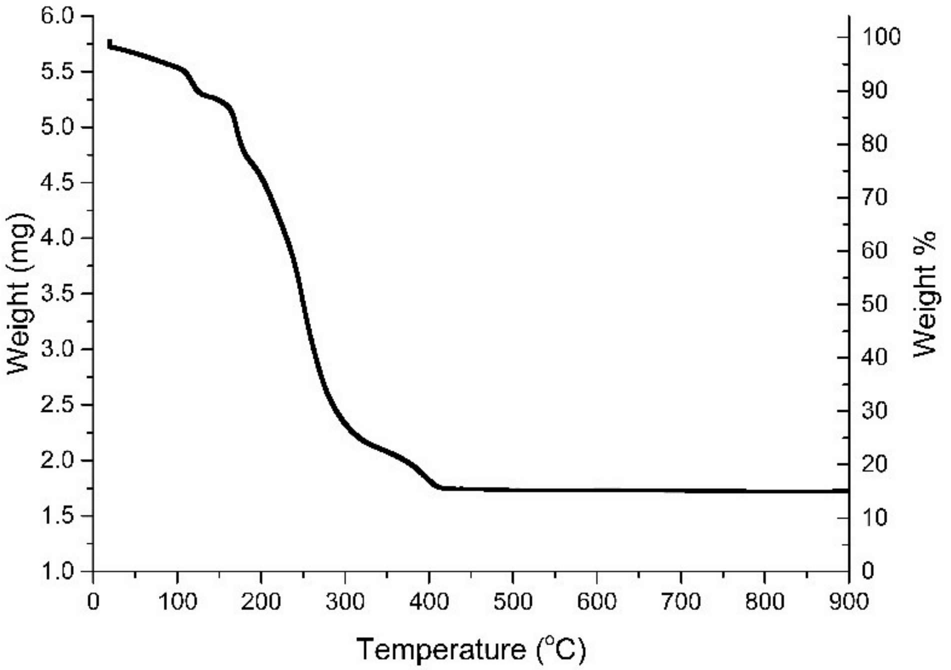

Fig. S2 TGA analysis of **Mn_8K_2**. The initial thermogravimetric steps up to ~150 ˚C can be attributed to the loss of constitutional and coordinating solvent molecules. The next step up to ~190 ˚C results from decomposition of two monodentate pivalates followed by the loss of 14 pivalate ligands resulting in the formation of Mn oxide materials.

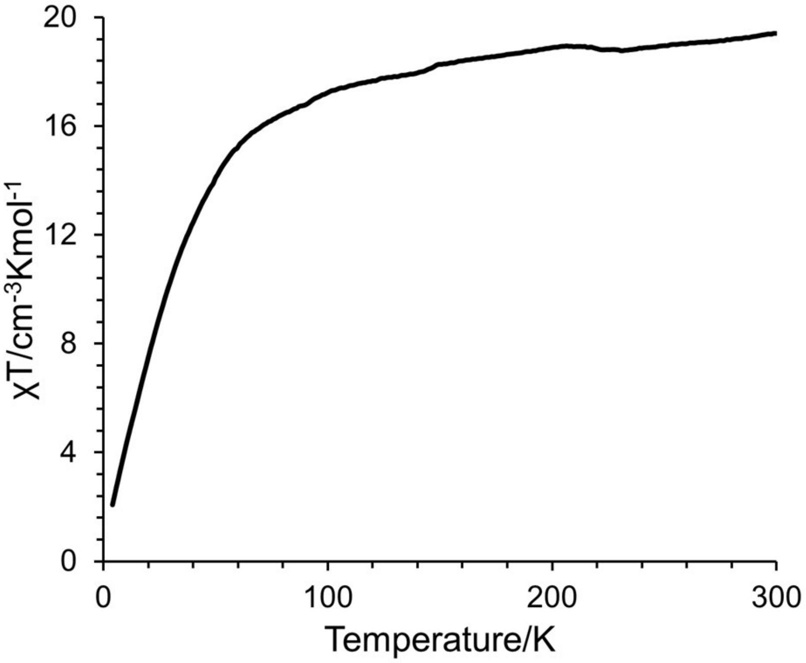

Fig. S3 Temperature-dependence of magnetic susceptibility for **Mn_8K_2**.

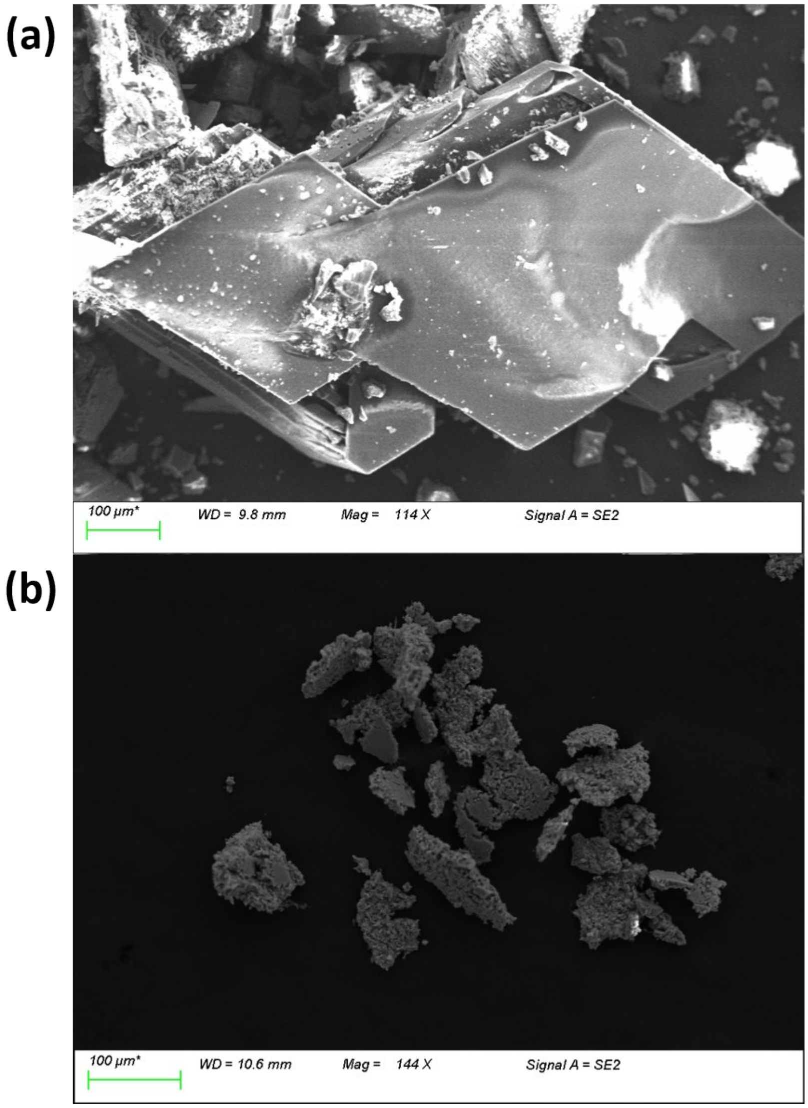

Fig. S4 SEM images of (**a**) **Mn_8K_2** and (**b**) **Mn_8K_2***. These images highlight the crystalline and amorphous nature of **Mn_8K_2** and **Mn_8K_2*** respectively.

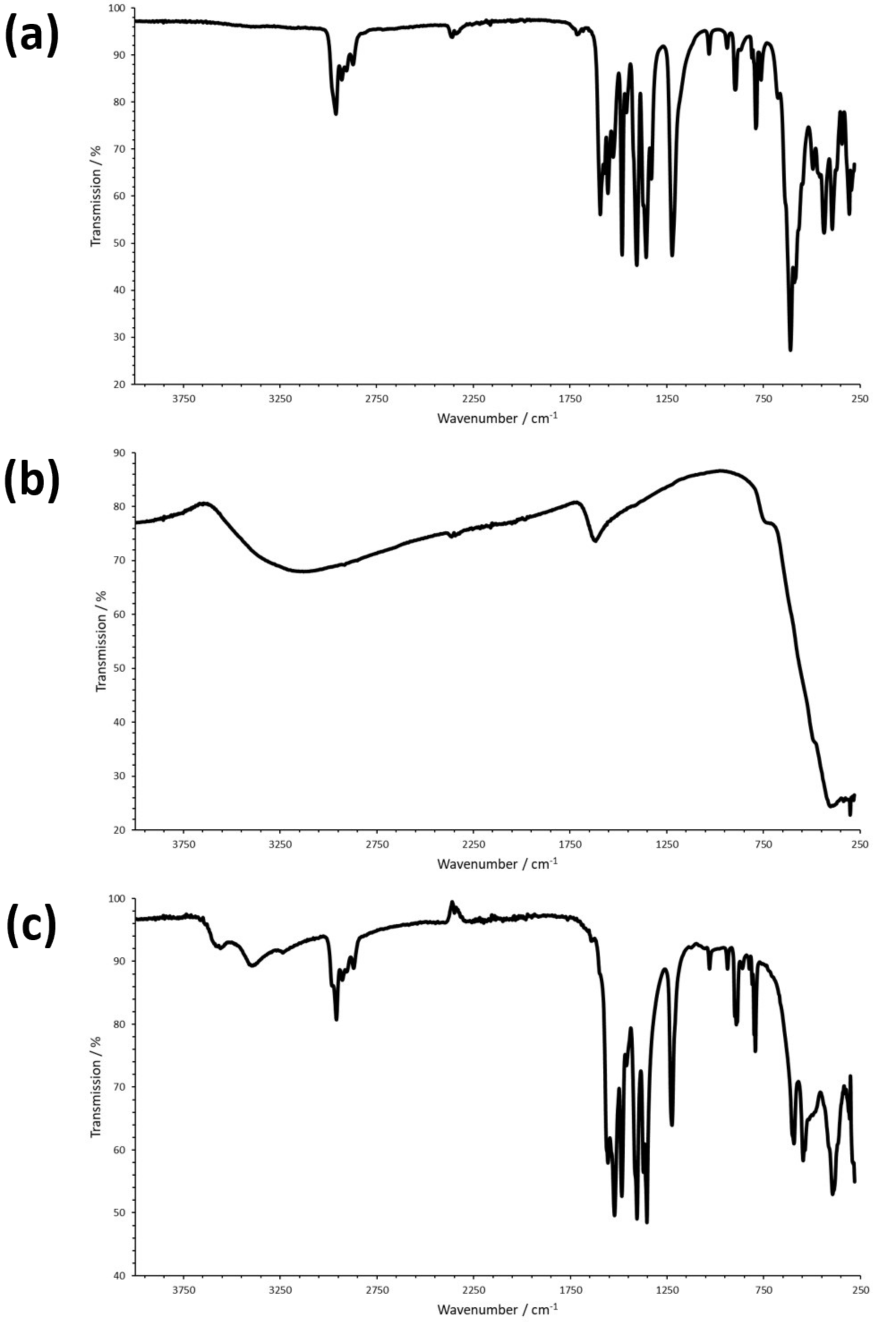

Fig. S5 IR spectrum of (**a**) **Mn_8K_2**, (**b**) **Mn_8K_2***, and (**c**) the precipitate obtained by evaporating the filtrate obtained after sonicating **Mn_8K_2** in water. (**a**) and (**b**) together highlight the differences in the structural characteristics of **Mn_8K_2** and **Mn_8K_2*** while (**c**) suggests the apparent formation of Mn pivalate species in solution.

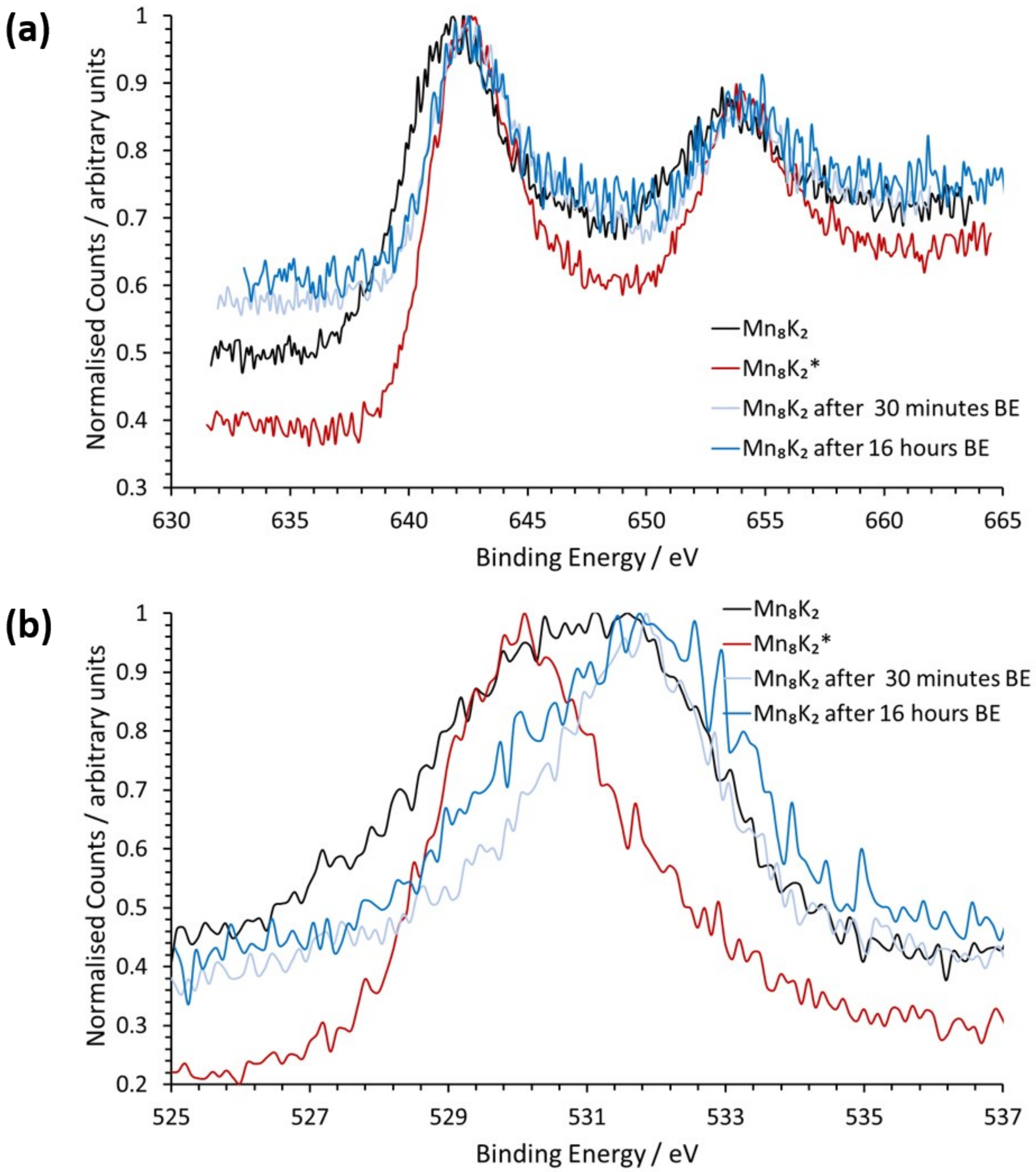

Fig. S6 (**a**) Mn 2p and (**b**) O 1s binding energies for **Mn_8K_2**, **Mn_8K_2*** and **Mn_8K_2/CP** after chronoamperometry. The O1s peak of **Mn_8K_2*** is centred at ~530.0 eV which relates to the O1s peak observed for Mn oxides. The O1s peaks for **Mn_8K_2** after bulk electrolysis are less intensive due to the lower sample quantities. The spectral variations of the O1s profiles for **Mn_8K_2*** and **Mn_8K_2** after catalysis, most likely reflect a variable degree of protonation of coordinating O-donor species, including O^{2-}, OH^- and H_2O species.

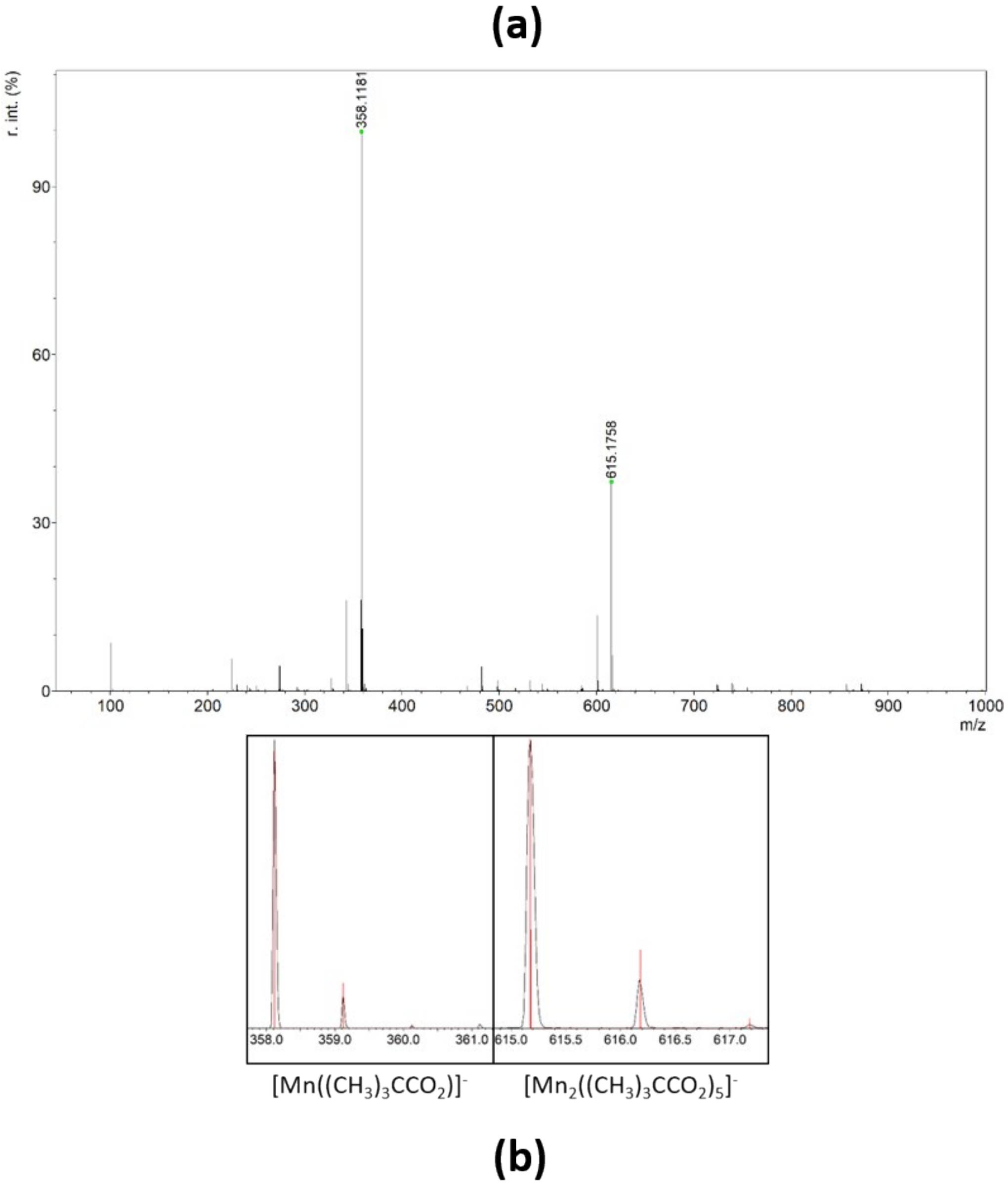

Fig. S7 ESI-mass spectrum of (**a**) the filtrate obtained after sonicating **Mn_8K_2** in water and (**b**) the assigned fragmentation pattern.

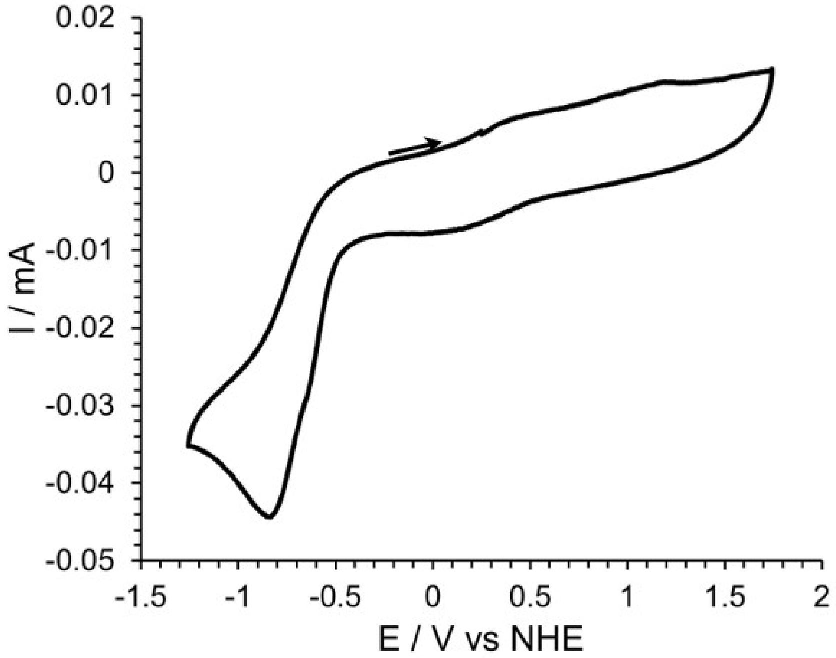

Fig. S8 Cyclic voltammogram for **Mn_8K_2** in dry acetonitrile. The arrow indicates the scan direction. The electrochemical behaviour of **Mn_8K_2** under these conditions resembles that of the synthetic {Mn_4Ca} complex reported previously[6] which suggests that **Mn_8K_2** is electronically similar to the OEC.

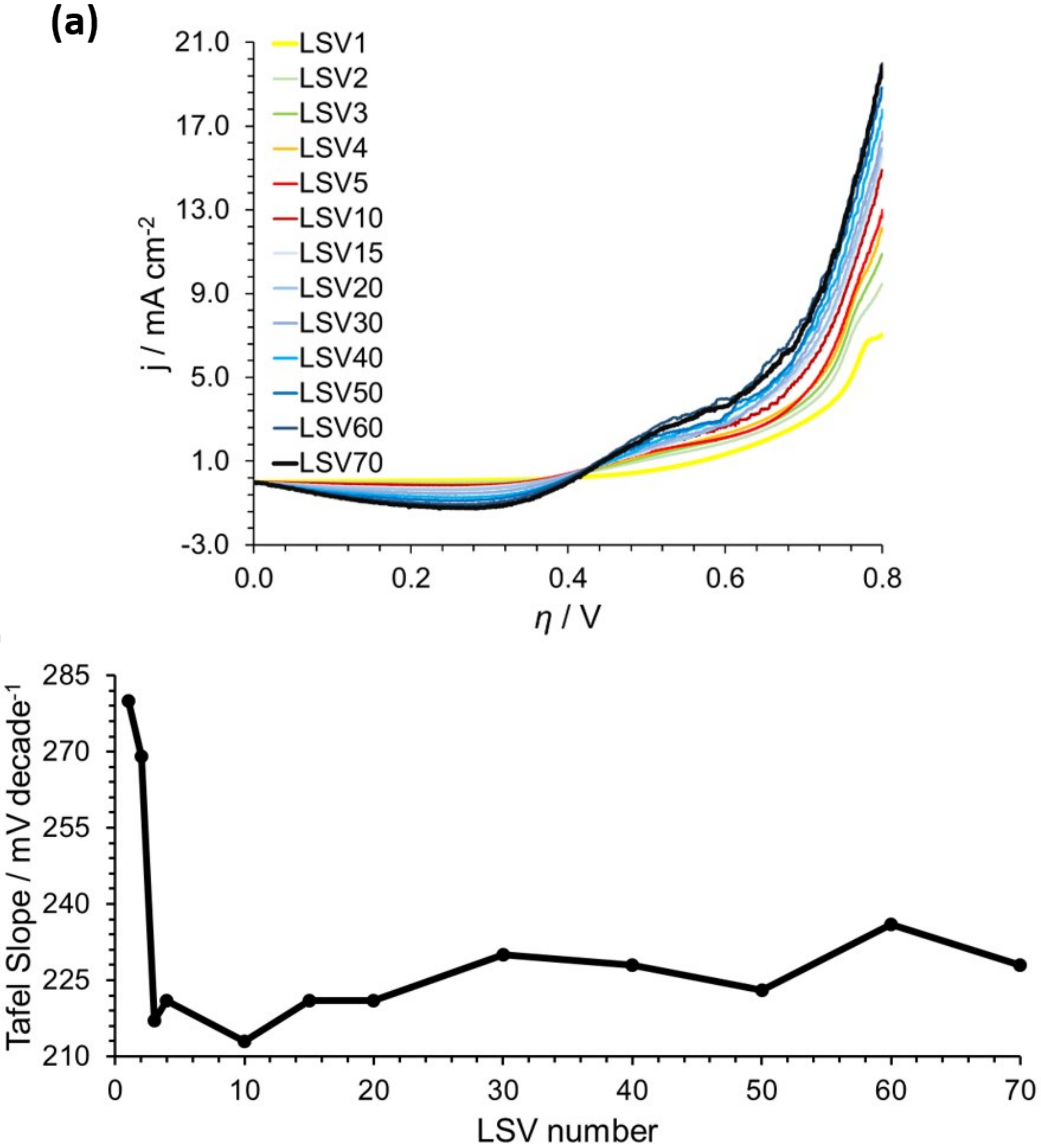

Fig. S9 (**a**) Successive linear sweep voltammograms for **Mn_8K_2/CP**. (**b**) Change in Tafel slope with successive LSV scans for **Mn_8K_2/CP** in the 700-800 mV overpotential range.

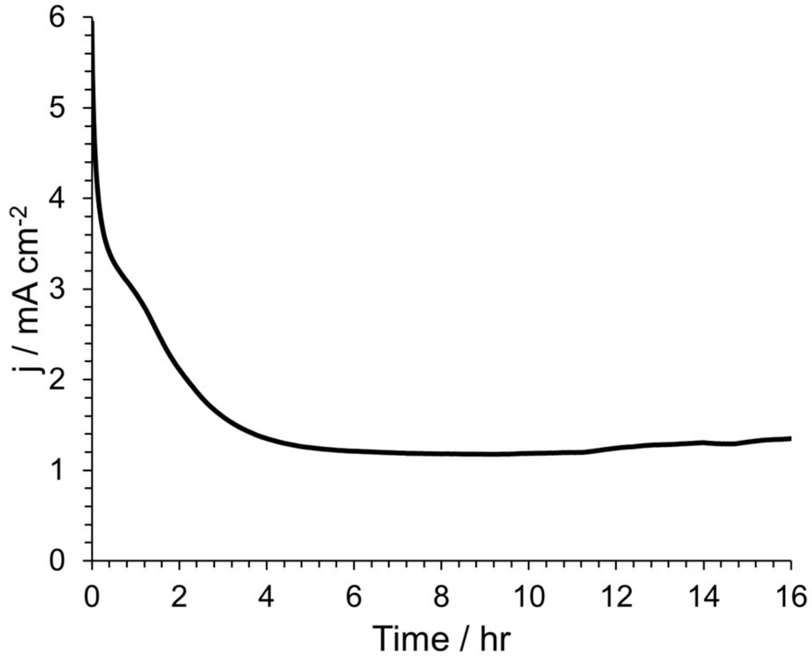

Fig. S10 CA data for **Mn_8K_2/CP** at 1.56 V *vs* NHE in KP*i* buffer at pH 7.2.

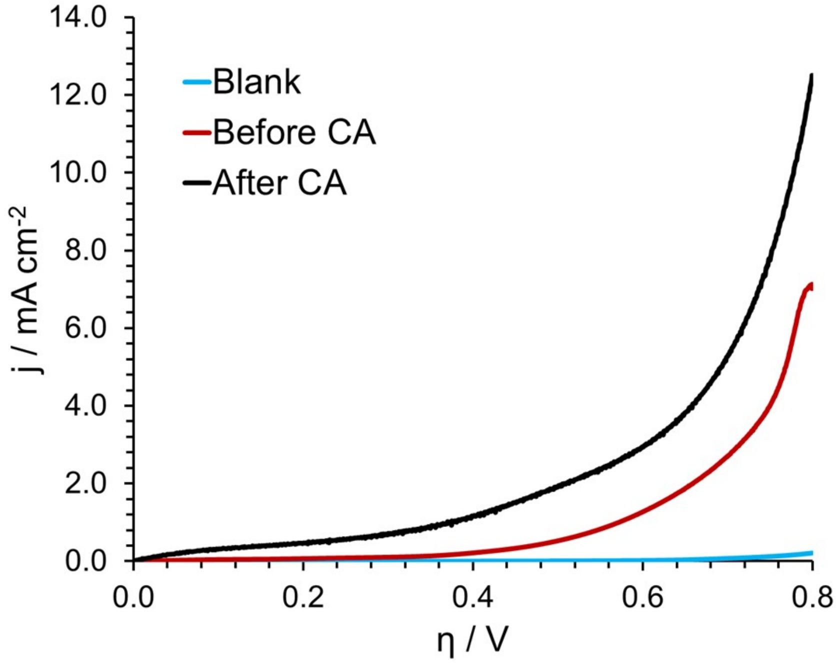

Fig. S11 Linear sweep voltammograms for **Mn_8K_2/CP** before and after a 16 hours long chronoamperometry experiment.

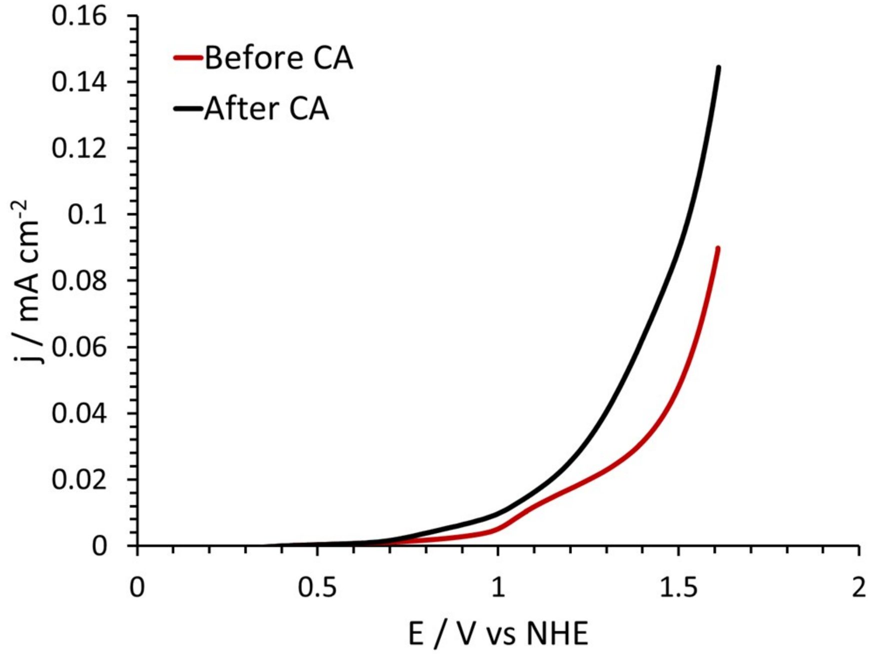

Fig. S12 Linear sweep voltammogram using a glassy carbon electrode in the solution used for chronoamperometry before and after chronoamperometry. A small increase can be observed in the current density from 0.09 mA cm^{-2} to 0.16 mA cm^{-2} at 1.6 V (vs NHE). This shows that there is small amount of leaching. However, the activity observed cannot be associated with the leached product as this increase is negligible compared to the current densities observed for **Mn_8K_2** and Mn_2O_3.

Computational Studies

Calculation of Coupling constants

DFT calculations were carried out using Gaussian09[7] package. We simplified the structure slightly by replacing the *tert*-butyl groups with methyl groups (Fig. S13). The calculations were performed using hybrid DFT functional PBE0[8] in conjunction with SDDALL[9] basis set having an effective core potential for the Mn and K atoms (replacing the 10 core electrons – $1s^22s^22p^6$ – of Mn and K with fully relativistic pseudopotentials), the 6-31G(d)[10] for C, N and O and 6-31G(p)[10] basis set for H.

For the ferromagnetic configuration, ground state geometry optimisation was performed using berny optimiser[11] as implemented in gaussian09.[7] The optimisation was carried out to the default convergence criteria using a large grid containing 225 radial shells with each shell containing 974 angular points as implemented in gaussian09.[7] For modelling the non-ferromagnetic configurations, broken symmetry calculations[12] were performed. For these calculations, the corresponding ferromagnetic state was used as the initial guess. It was ensured that in each case the overall multiplicity of the system was positive. The wavefunction was then analysed to look for instabilities[13] and optimised until a stable wavefunction was found. This wavefunction was then employed for the final geometry optimisation using the berny optimiser.[11] A smaller step size (0.01 Bohr) and a tighter convergence criterion for SCF ($\Delta_{energy} < 10^{-11}$ Hartrees) was used to facilitate finding the ground state on a flat potential energy surface due to the presence of methyl groups.

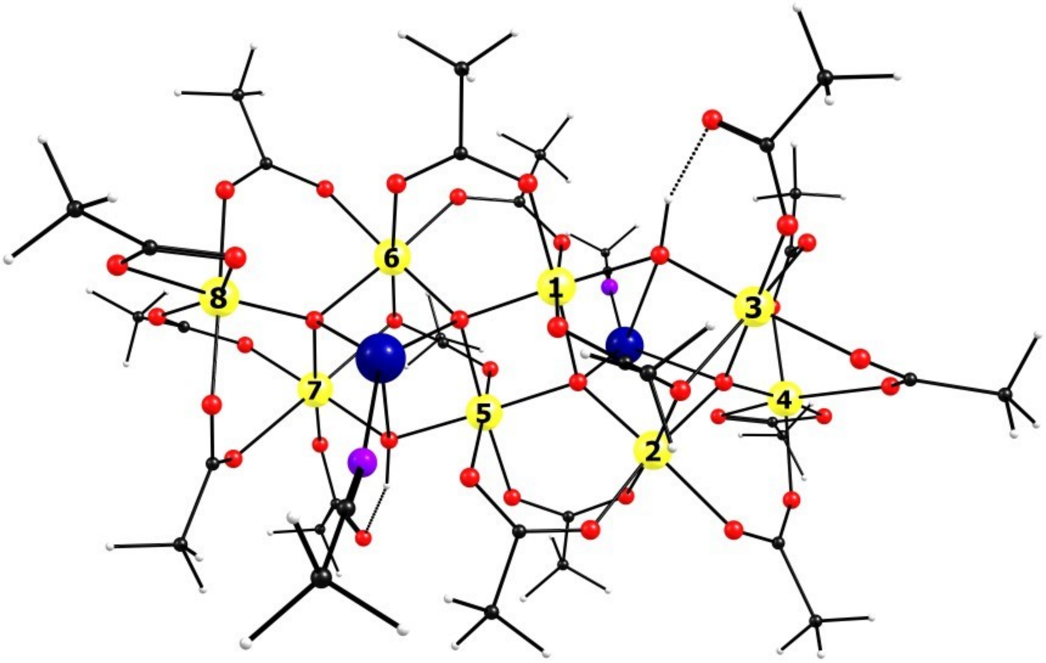

Fig. S13 Computational model for **Mn_8K_2**. Mn, K, C, N, O and H are shown in yellow, purple, black, blue, red and light grey respectively. The number on each Mn centre is the number used for referring to each Mn centre.

Validation of the computational model and the calculation of coupling constants

The formal oxidation states of each Mn centre was assumed to be +III. The bond distances for the calculates states were then compared with the single crystal X-ray data and a very good agreement was found. Thus, the formal oxidation state of each Mn centre in $\mathbf{Mn_8K_2}$ is +III. A comparison of some selected distances in a single cubane unit (derived from the symmetric ‘ferromagnetic’ structure in which all spins are parallel aligned) is provided in Table S3. Since the complex contains an inversion centre, the environments of Mn1-Mn4 are identical to that of Mn5-Mn8 and thus, the distances for only Mn1-Mn4 have been presented in Table S3.

The applied approach involves the spin-inversion at various Mn sites, thus breaking the spin symmetry whilst the initial structure is used for the calculations. The spin configuration of the 11 states that were modelled and the energies of these states are shown in Table S4. The symmetry of the complex is reduced on relaxation; however, the structural differences are relatively small. The resulting data demonstrates that the ‘ferromagnetic’ state is not the ground state in agreement with the experimental data.

For this complex, (8*(8-1)/2 =) 28 possible coupling constants were considered. It is assumed that the exchange coupling between closely-located, bridged Mn centres (that are linked to each other *via* carboxylate or oxo/hydroxo-groups) is stronger compared to the coupling between Mn centres that are not directly linked. Based on these considerations and the symmetry of the structure, the following Hamiltonian was applied:

$$\begin{aligned} H = &-2J_1\langle s_1.s_5\rangle - 2J_2\left[\langle s_1.s_2\rangle + \langle s_5.s_6\rangle\right] - 2J_3\left[\langle s_1.s_3\rangle + \langle s_5.s_7\rangle\right] - 2J_4\left[\langle s_1.s_6\rangle + \langle s_2.s_5\rangle\right] \\ &- 2J_5\left[\langle s_2.s_3\rangle + \langle s_6.s_7\rangle\right] - 2J_6\left[\langle s_2.s_4\rangle + \langle s_6.s_7\rangle\right] - 2J_7\left[\langle s_3.s_4\rangle + \langle s_7.s_8\rangle\right] \end{aligned}$$

For calculating the J-values, the methodology described by Paul and Mishra[14] was employed and the spin operators were defined using the spin densities obtained from Bader charge analysis.[15] The spin densities obtained for each Mn centres in the different spin states are given in Table S5. For calculating 7 coupling constants, 8 spin states need to be modelled. To remove any dependence of the coupling constants on the spin state, we modelled 11 spin states and the code ej_calc was used to calculate the coupling constants. The code details and the applied methodology are described in Ref. 16. The methodology can be briefly described as follows. Since more spin states (11) have been modelled than required (8), there exist more than one solution, i.e. the solution is overspecified. All possible solutions were calculated and the singular solutions were discarded. The average and the standard deviation for each coupling constant was calculated for the non-singular solutions obtained. The solutions in which any of the coupling constant was deviating by more than three standard deviations was discarded and the average and the standard deviation were recalculated with the cycle repeated until self-consistency. The coupling constants obtained this way are provided in Table S6 and they were found to reproduce the relative energy of the modelled spin states within an error of 3%. It can be seen that the strongest coupling is antiferromagnetic and is between Mn1 and Mn5. The coupling within the cubane unit is dominantly ferromagnetic.

The dimension of the Hamiltonian matrix was too large (Ms = 5, therefore, $5^8 \times 5^8$ i.e. 390625×390625) for exact diagonalisation, so the magnetic susceptibility was not determined from the coupling constants. Using the J-values and the above mentioned Hamiltonian however, the energies of the different spin states were determined. The spin operators for the Hamiltonian were determined by taking an average of the spin densities in the different electronic states that were modelled. This was also achieved using ej_calc.[16] The energy of all $2^{(8-1)}$ (=128) unique spin states are provided in Table S7. The ground state was determined to be an S = 0 state where the spin on Mn1, Mn2, Mn3 and Mn4 is opposite to that on the other Mn centres. The ferromagnetic state was found to be 657 cm^{-1} above the ground state.

<u>Investigation of the initiation mechanism</u>

In order to investigate how the OER catalysis is initiated by **Mn_8K_2**, the substitution of pivalate groups with water molecules and OH^- ions was computationally investigated. The parameters used for the calculation of coupling constants were used for this purpose as well. The whole complex with the *tert*-butyl groups replaced with methyl groups was used as a model again to avoid irregular truncations. The solvent environment of water was modelled using the PCM model.[17] For each model, only the ferromagnetic state was modelled and frequency calculations were performed to determine the free energies.

Considering the presence of excess water under the conditions in which catalysis was investigated, it is likely that the CH_3CN molecule attached to K^+ ion will be replaced by a water molecule. The substitution of both CH_3CN molecules was found to require ~23 kJ/mol which indicates that this will occur easily under the conditions employed for the determination of the catalytic activity. The investigation of the substitution of pivalate groups was therefore investigated with a model containing water molecules (instead of CH_3CN molecules) attached to the K^+ ions although with further modifications were introduced on one of the monomeric units.

The structural features of this complex suggest that the substitution of the monodentate pivalate group bound to Mn3 should be the easiest. Since this is hydrogen bonded to the μ-OH^- group, O3, it can potentially be removed as a pivalic acid molecule either via a proton transfer from O3 or from the surrounding water molecules. To investigate the former possibility, we modelled the transfer of the proton from O3 to the pivalate group (Fig. S14(a)). This however, was found to be highly endothermic (~82 kJ/mol) illustrating the energy intensive nature of this pathway. For investigating the latter possibility, the system was modelled with the pivalate replaced with a OH^- (Fig. S14(b)). This substitution was found to be highly favourable (stabilisation energy: ~181 kJ/mol) which suggests that Mn3 may potentially serve as an initial attack site for water molecules. There may still be a barrier for substitution but the high thermodynamic and entropic favourability should drive this substitution forward.

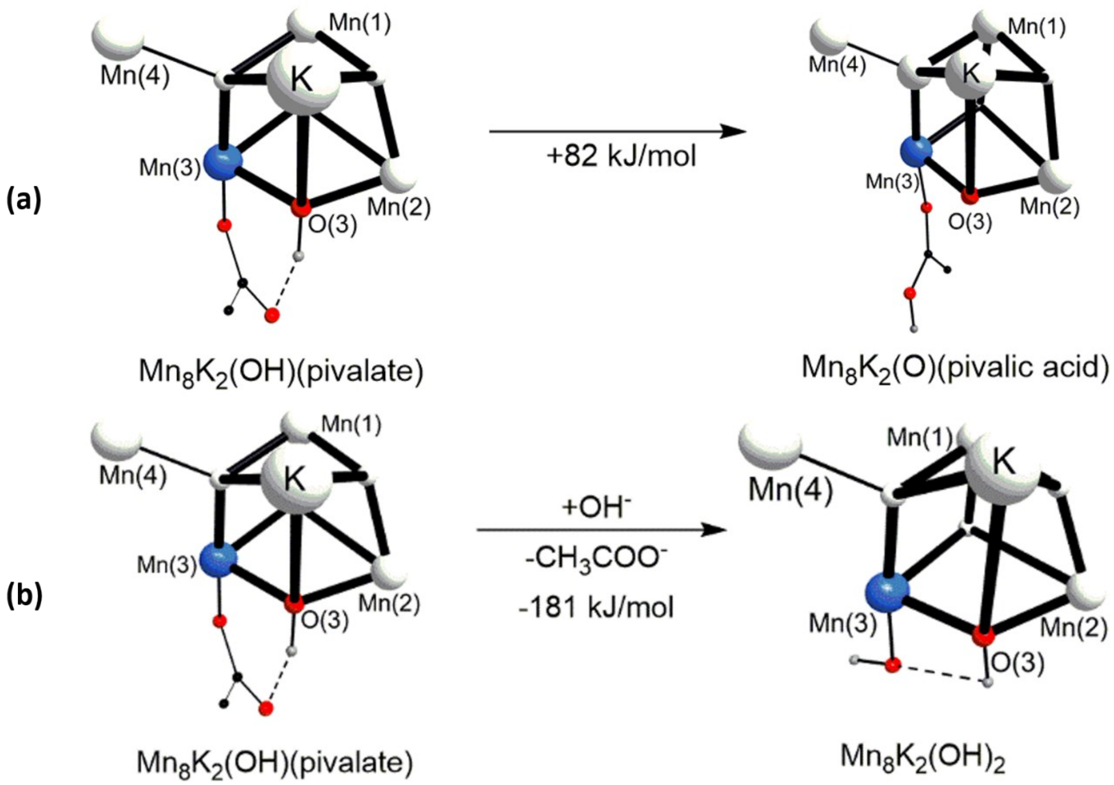

Fig. S14 Representation of (**a**) the proton transfer mechanism and (**b**) the substitution of the pivalate group with an OH^- group as calculated using DFT.

Table S3 Comparison of selected metal-metal distances (Å) obtained from the crystal structure of **Mn_8K_2** and from DFT calculations for the symmetric 'ferromagnetic' state in which all spins adopt a parallel arrangement. The crystal structure and the optimised ferromagnetic state are both characterised by inversion symmetry, whereby only four Mn centres (Mn1-Mn4) adopt unique atom positions. The close agreement between the experimental and the calculated distances suggest that the model represents the experimental structure well and that the oxidation states are correct. Note: The atom numbering is consistent with that presented in Fig. S13.

	XRD	*Model (ferromagnetic state)*
Mn1-Mn2	3.40	3.41
Mn1-Mn3	3.48	3.48
Mn1-Mn4	5.34	5.28
Mn1-Mn5	2.85	2.88
Mn2-Mn3	3.10	3.13
Mn2-Mn4	3.33	3.37
Mn3-Mn4	3.28	3.26
K-Mn1	3.62	3.68
K-Mn2	3.71	3.67
K-Mn3	4.21	4.44
K-Mn4	3.46	3.49

Table S4 Spin configurations and associated relative energies that were modelled using DFT in order to determine the magnetic exchange coupling constants for **Mn_8K_2**.

Configuration (Mn1-Mn8; see Fig. S13)	*Energy (cm^{-1}) relative to the ferromagnetic state*
↑↑↓↑↑↑↑↑	163.251
↑↓↑↑↑↑↑↑	136.468
↑↑↑↑↑↑↑↑	0
↓↓↑↑↑↓↑↑	-75.786
↓↓↓↑↑↓↑↑	-287.538
↓↓↑↑↑↑↑↓	-370.527
↓↑↓↑↑↑↑↑	-395.623
↓↑↑↓↑↑↑↑	-460.949
↓↓↓↑↑↑↓↑	-463.211
↓↓↑↓↑↑↑↑	-503.945
↓↓↓↑↑↑↑↓	-584.808

Note: The arrows correspond to the spin configurations of Mn1-Mn8 as shown in Fig. S13. The corresponding optimised structures lose their inversion symmetry, except for the symmetric ↑↑↑↑↑↑↑↑ state (see provided optimised coordinates).

Table S5 Spin densities on Mn centres in different spin states and the relative energy (cm^{-1}) of each modelled state relative to the 'ferromagnetic' state for **Mn$_8$K$_2$**. Note: The atom numbering is consistent with that presented in Fig. S13. The spin-configurations correspond to the arrow representations in Table S4.

Mn1	*Mn2*	*Mn3*	*Mn4*	*Mn5*	*Mn6*	*Mn7*	*Mn8*	*Relative Energy (cm^{-1})*
3.81836	3.85166	-3.80951	3.84350	3.82996	3.86187	3.85767	3.85741	163.251
3.81107	-3.79427	3.84852	3.83546	3.81762	3.86202	3.85821	3.85768	136.468
3.83005	3.86238	3.85804	3.85778	3.83026	3.86244	3.85825	3.85770	0
-3.81068	-3.81225	3.83306	3.83558	3.79344	-3.81060	3.84913	3.83474	-75.786
-3.82253	-3.82181	-3.83538	3.82255	3.79270	-3.81070	3.84923	3.83479	-287.538
-3.79976	-3.81202	3.83337	3.83561	3.81164	3.82208	3.83534	-3.82244	-370.527
-3.79179	3.83227	-3.82702	3.84272	3.82313	3.84471	3.85794	3.85735	-395.623
-3.77998	3.82038	3.81919	-3.82287	3.82284	3.84508	3.85798	3.85765	-460.949
-3.81109	-3.82187	-3.83540	3.82240	3.79998	3.83357	-3.80991	3.84364	-463.211
-3.79964	-3.83351	3.81022	-3.84363	3.81153	3.84515	3.85810	3.85751	-503.945
-3.81111	-3.82148	-3.83560	3.82232	3.81108	3.82149	3.83565	-3.82227	-584.808

Table S6 Resulting J-values (cm^{-1}) calculated using DFT and the Mn-Mn interactions that constitute each J-value for **Mn_8K_2**. The standard deviations for the resulting J values are small, justifying the choice of Hamiltonian. The J values are consistent with the symmetry of the structure as determined by single-crystal X-ray diffraction.

J-value	*Interacting Mn centres*	*Magnitude (cm^{-1})*
J_1	Mn1-Mn5	-31.40 ± 0.76
J_2	Mn1-Mn2 Mn5-Mn6	1.74 ± 0.48
J_3	Mn1-Mn3 Mn5-Mn7	2.24 ± 0.48
J_4	Mn1-Mn6 Mn2-Mn5	-6.89 ± 0.43
J_5	Mn2-Mn3 Mn6-Mn7	10.24 ± 0.32
J_6	Mn2-Mn4 Mn6-Mn8	4.10 ± 0.40
J_7	Mn3-Mn4 Mn7-Mn8	-1.73 ± 0.50

Table S7 The relative energies (cm^{-1}) with respect to the ground state for all the possible spin configurations for **Mn_8K_2** calculated using the J-values and the average Bader spin densities for each Mn centre. Degenerate mirror configurations are not shown.

Configuration	*Energy*	*Configuration*	*Energy*	*Configuration*	*Energy*
↑↑↑↑↓↓↓↓	0	↑↓↑↓↓↑↑↑	410	↑↓↑↓↑↑↑↓	742
↑↑↑↓↓↓↓↓	35	↑↓↓↓↓↑↓↑	411	↑↑↑↓↑↓↑↓	742
↑↑↑↑↓↓↓↑	35	↑↑↓↓↓↑↑↓	437	↑↓↑↑↑↓↓↓	750
↑↑↑↓↓↓↓↑	70	↑↓↓↑↓↓↑↑	438	↑↓↓↓↑↓↑↑	751
↑↑↓↑↓↓↓↓	158	↑↓↑↓↓↑↑↓	445	↑↓↑↓↑↓↑↓	757
↑↑↑↑↓↓↑↓	159	↑↓↓↑↓↑↓↑	445	↑↑↓↑↑↓↓↓	773
↑↓↓↓↓↓↓↓	159	↑↑↓↓↓↓↑↑	488	↑↓↓↓↑↑↓↑	774
↑↑↑↑↓↑↑↑	159	↑↓↑↑↓↓↑↓	495	↑↓↑↑↑↓↓↑	785
↑↑↓↑↓↓↓↑	192	↑↑↓↓↓↑↓↑	495	↑↓↓↑↑↓↑↑	786
↑↑↑↓↓↓↑↓	193	↑↓↑↑↓↑↑↑	495	↑↓↑↑↑↑↑↑	792
↑↓↓↑↓↓↓↓	193	↑↓↑↓↓↓↑↑	495	↑↑↑↑↑↓↑↑	794
↑↓↓↓↓↓↓↑	194	↑↑↓↑↓↑↓↓	496	↑↑↓↑↑↓↓↑	807
↑↑↑↓↓↑↑↑	194	↑↓↓↓↓↑↓↓	497	↑↓↓↑↑↑↓↑	808
↑↑↑↑↓↑↑↓	194	↑↓↑↓↓↑↓↑	503	↑↑↓↑↑↑↑↑	815
↑↓↓↑↓↓↓↑	228	↑↓↑↑↓↑↑↓	530	↑↑↑↑↑↑↓↑	816
↑↑↑↓↓↑↑↓	229	↑↓↓↑↓↑↓↓	531	↑↓↑↑↑↑↑↓	827
↑↑↓↓↓↓↓↓	243	↑↓↓↓↑↓↓↓	573	↑↑↑↓↑↓↑↑	828
↑↑↑↑↓↓↑↑	245	↑↓↑↑↓↓↑↑	581	↑↓↑↑↑↓↑↓	843
↑↓↑↓↓↓↓↓	251	↑↑↓↓↓↑↓↓	581	↑↓↑↓↑↓↑↑	843
↑↑↑↑↓↑↓↑	252	↑↓↑↑↓↑↓↑	588	↑↑↓↑↑↑↑↓	850
↑↑↓↓↓↓↓↑	278	↑↓↑↓↓↑↓↓	589	↑↑↑↓↑↑↓↑	851
↑↑↑↓↓↓↑↑	279	↑↓↓↑↑↓↓↓	607	↑↑↓↓↑↓↓↓	858
↑↓↑↓↓↓↓↑	286	↑↓↓↓↑↓↓↑	608	↑↓↓↓↑↑↓↓	860
↑↑↑↓↓↑↓↑	287	↑↓↓↓↑↑↑↑	615	↑↑↓↑↑↓↑↓	865
↑↑↓↑↓↓↑↓	316	↑↑↑↑↑↓↓↓	615	↑↓↑↓↑↑↓↑	866
↑↑↓↑↓↑↑↑	317	↑↓↓↑↑↓↓↑	642	↑↑↓↓↑↓↓↑	893
↑↓↓↓↓↓↑↓	318	↑↓↓↑↑↑↑↑	650	↑↓↓↑↑↑↓↓	894
↑↓↓↓↓↑↑↑	318	↑↑↑↓↑↓↓↓	650	↑↑↓↓↑↑↑↑	900
↑↓↑↑↓↓↓↓	336	↑↓↓↓↑↑↑↓	650	↑↑↑↑↑↑↓↓	902
↑↑↑↑↓↑↓↓	338	↑↑↑↑↑↓↓↑	650	↑↓↑↑↑↓↑↑	929
↑↑↓↑↓↑↑↓	352	↑↑↑↑↑↑↑↑	657	↑↑↓↓↑↑↑↓	935
↑↓↓↑↓↓↑↓	352	↑↓↑↓↑↓↓↓	665	↑↑↑↓↑↑↓↓	937
↑↓↓↑↓↑↑↑	353	↑↓↓↓↑↓↑↓	665	↑↑↓↓↑↓↑↓	951
↑↓↓↓↓↑↑↓	353	↑↓↑↑↓↑↓↓	674	↑↓↑↑↑↑↓↑	951
↑↓↑↑↓↓↓↑	371	↑↓↓↑↑↑↑↓	684	↑↑↓↑↑↓↑↑	951
↑↑↑↓↓↑↓↓	373	↑↑↑↓↑↓↓↑	685	↑↓↑↓↑↑↓↓	952
↑↓↓↑↓↑↑↓	388	↑↑↑↓↑↑↑↑	692	↑↑↓↑↑↑↓↑	974
↑↑↓↓↓↓↑↓	402	↑↑↑↑↑↑↑↓	692	↑↑↓↓↑↓↑↑	1037
↑↑↓↓↓↑↑↑	402	↑↓↑↓↑↓↓↑	699	↑↓↑↑↑↑↓↓	1037
↑↑↓↑↓↓↑↑	402	↑↓↓↑↑↓↑↓	700	↑↑↓↓↑↑↓↑	1059
↑↓↓↓↓↓↑↑	403	↑↓↑↓↑↑↑↑	707	↑↑↓↑↑↑↓↓	1060
↑↓↑↓↓↓↑↓	409	↑↑↑↑↑↓↑↓	708	↑↑↓↓↑↑↓↓	1145
↑↑↓↑↓↑↓↑	410	↑↑↑↓↑↑↑↓	727		

References

1 Bruker, *SADABS, Bruker AXS Inc., Madison, Wisconsin, USA*, 2001.

2 O. V. Dolomanov, L. J. Bourhis, R. J. Gildea, J. A. K. Howard and H. Puschmann, *J. Appl. Crystallogr.*, 2009, **42**, 339-341.

3 G. M. Sheldrick, *Acta Crystallogr. A*, 2015, **71**, 3-8.

4 G. M. Sheldrick, *Acta Crystallogr. A*, 2008, **64**, 112-122.

5 B. H. Toby, *Powder Diffr.*, 2012, **21**, 67-70.

6 C. X. Zhang, C. H. Chen, H. X. Dong, J. R. Shen, H. Dau and J. Q. Zhao, *Science*, 2015, **348**, 690-693.

7 M. J. T. Frisch, G. W.; Schlegel, H. B.; Scuseria, G. E.; Robb, M. A.; Cheeseman, J. R.; Scalmani, G.; Barone, V.; Mennucci, B.; Petersson, G. A.; Nakatsuji, H.; Caricato, M.; Li, X.; Hratchian, H. P.; Izmaylov, A. F.; Bloino, J.; Zheng, G.; Sonnenberg, J. L.; Hada, M.; Ehara, M.; Toyota, K.; Fukuda, R.; Hasegawa, J.; Ishida, M.; Nakajima, T.; Honda, Y.; Kitao, O.; Nakai, H.; Vreven, T.; Montgomery, J. A., Jr.; Peralta, J. E.; Ogliaro, F.; Bearpark, M.; Heyd, J. J.; Brothers, E.; Kudin, K. N.; Staroverov, V. N.; Kobayashi, R.; Normand, J.; Raghavachari, K.; Rendell, A.; Burant, J. C.; Iyengar, S. S.; Tomasi, J.; Cossi, M.; Rega, N.; Millam, J. M.; Klene, M.; Knox, J. E.; Cross, J. B.; Bakken, V.; Adamo, C.; Jaramillo, J.; Gomperts, R.; Stratmann, R. E.; Yazyev, O.; Austin, A. J.; Cammi, R.; Pomelli, C.; Ochterski, J. W.; Martin, R. L.; Morokuma, K.; Zakrzewski, V. G.; Voth, G. A.; Salvador, P.; Dannenberg, J. J.; Dapprich, S.; Daniels, A. D.; Farkas, Ö.; Foresman, J. B.; Ortiz, J. V.; Cioslowski, J.; Fox, D. J. , *Gaussian 09, Revision D.01*, 2009.

8 (a) J. P. Perdew, K. Burke and M. Ernzerhof, *Phys. Rev. Lett.*, 1996, **77**, 3865-3868; (b) C. Adamo and V. Barone, *J. Chem. Phys.*, 1999, **110**, 6158-6170.

9 M. Dolg, U. Wedig, H. Stoll and H. Preuss, *J. Chem. Phys.*, 1987, **86**, 866-872.

10 M. M. Francl, W. J. Pietro, W. J. Hehre, J. S. Binkley, M. S. Gordon, D. J. Defrees and J. A. Pople, *J. Chem. Phys.*, 1982, **77**, 3654-3665.

11 H. B. Schlegel, *J. Comp. Chem.*, 1982, **3**, 214-218.

12 (a) A. P. Ginsberg, *J. Am. Chem. Soc.*, 1980, **102**, 111-117; (b) L. Noodleman, *J. Chem. Phys.*, 1981, **74**, 5737-5743; (c) L. Noodleman, D. A. Case and A. Aizman, *J. Am. Chem. Soc.*, 1988, **110**, 1001-1005; (d) E. Ruiz, J. Cano, S. Alvarez and P. Alemany, *J. Comp. Chem.*, 1999, **20**, 1391-1400.

13 R. Bauernschmitt and R. Ahlrichs, *J. Chem. Phys.*, 1996, **104**, 9047-9052.

14 S. Paul and A. Misra, *J. Chem. Theory Comput.*, 2012, **8**, 843-853.

15 (a) R. F. W. Bader, *Atoms in Molecules: a Quantum Theory*, Clarendon Press, 1990; (b) M. Yu and D. R. Trinkle, *J. Chem. Phys.*, 2011, **134**.

16 S. Tandon, M. Venkatesan, W. Schmitt and G. W. Watson, *Dalton Trans.*, 2020, DOI: 10.1039/D0DT01404D.

17 G. Scalmani and M. J. Frisch, *J. Chem. Phys.*, 2010, **132**, 114110.